Title	A Conventional straddle-sliding-packer system as a borehole extensometer; Monitoring shear displacement of a fault during an injection test
Author(s)	Ishii Eiichi
Citation	Engineering Geology,275,p.105748_1-105748_12
Text Version	Published Journal Article
URL	https://jopss.jaea.go.jp/search/servlet/search?5066005
DOI	https://doi.org/10.1016/j.enggeo.2020.105748
Right	© 2020 The Author. Published by Elsevier B.V. This is an open access article under the CC BY license (http://creativecommons.org/licenses/BY/4.0/).

Engineering Geology 275 (2020) 105748

Contents lists available at ScienceDirect

Engineering Geology

journal homepage: www.elsevier.com/locate/enggeo

A conventional straddle-sliding-packer system as a borehole extensometer: Monitoring shear displacement of a fault during an injection test

Eiichi Ishii

Horonobe Underground Research Center, Japan Atomic Energy Agency, Horonobe-cho, Japan

ARTICLE INFO

Keywords:
Borehole extensometer
Fault displacement
Hydraulic dilation angle
Injection test
Siliceous mudstone
Sliding packer

ABSTRACT

A constant-head step injection test using a conventional straddle-packer system was performed for a normal fault in siliceous mudstone. The test applied a new method whereby axial displacements of isolated test sections in a borehole during injection are monitored by measuring the pressures of sliding packers and the pore pressure in the test section. The measured pressures and axial displacement, and the injection flow rate, were used to estimate the hydraulic aperture, shear displacement, normal compliance, normal stress, shear stiffness and hydraulic dilation angle of the fault during the test. The injection successfully yielded a large shear displacement during normal faulting of up to 13.3–49.5 mm (including the estimation error), which left residual shear displacement of 2.8–10.4 mm after a remarkable shear-slip event. The shear stiffness during faulting is estimated to be 2.3×10^7 to 8.4×10^7 Pa m^{-1} (considering the estimation error), which is consistent with empirically predicted values based on previous studies. The hydraulic dilation angle was inferred to be effectively zero as the residual shear displacement did not leave any increase in hydraulic aperture. The experimental method applied here does not require specialized equipment and could aid in the investigation of the hydromechanical behavior of subsurface fractures or aquifers.

1. Introduction

The safe disposal of radioactive waste must consider host-rock permeability following closure of the underground repository. The host rock is likely to include some (minor) faults, whose transmissivities must be properly assessed. A conservative assessment must consider any possible increase in transmissivity that could occur following fault reactivation, for example caused by thermal-hydro-mechanically induced shear stresses and thermal pressurization due to the release of heat from radioactive waste (Birkholzera et al., 2019; Rutqvist, 2020; Rutqvist and Stephansson, 2003; Urpi et al., 2019).

According to the parallel-plate model (cubic law) of Snow (1968), the transmissivity T of a fracture (m s^{-2}) can be related to the hydraulic aperture of the fracture δ_H (m) as follows:

$$T = \rho_w g \delta_h^3 / 12\mu \quad (1)$$

where ρ_w is the density of water (kg m^{-3}), g is the acceleration due to gravity (m s^{-2}), and μ is the dynamic viscosity of water (Pa s). The hydraulic aperture increment $\Delta\delta_h$ (m) during shearing is expressed as follows:

$$\Delta\delta_h = \Delta u_s \tan(d_h) \quad (2)$$

where Δu_s is the shear displacement increment (m), and d_h is the dilation angle for hydraulic aperture (°) (McClure and Horne, 2014a). Therefore, if a fault is artificially sheared, in situ measurement of the hydraulic dilation angle at that time can help to assess a possible increase in the fault's transmissivity during fault reactivation.

Artificially induced fault reactivation due to increasing groundwater pressure has been observed in earthquakes that were triggered by wastewater fluid injection (Ellsworth, 2013; Healy et al., 1966; Hsieh and Bredehoeft, 1981). Recently, numerous injection activities have been carried out on a large scale for a variety of purposes such as geothermal exploitation, natural oil/gas production, and geological carbon storage, where artificially induced fault reactivation has been observed and focused in terms of seismic hazard (Davies et al., 2013; Dempsey et al., 2015; Evans et al., 2005; McClure and Horne, 2014b; Rutqvist et al., 2015; Tezuka and Niitsuma, 2000; Vilarrasa et al., 2019; Zakharova and Goldberg, 2014). Small-scale injection tests are also actively conducted in underground research laboratories, where detailed hydromechanical behavior of faults is carefully studied by artificially inducing fault reactivation (Guglielmi et al., 2015a, 2015b, 2017, 2020; Jeanne et al., 2018). Based on these previous activities/tests, small-scale injection testing is expected to be a useful technique to investigate the hydraulic dilation angle of faults (cf., Guglielmi et al., 2015b; Nguyen et al., 2019). However, measuring the shear displacement during injection typically requires specialized equipment such as

E-mail address: ishii.eiichi@jaea.go.jp.

https://doi.org/10.1016/j.enggeo.2020.105748
Received 29 April 2020; Received in revised form 22 June 2020; Accepted 24 June 2020
Available online 27 June 2020

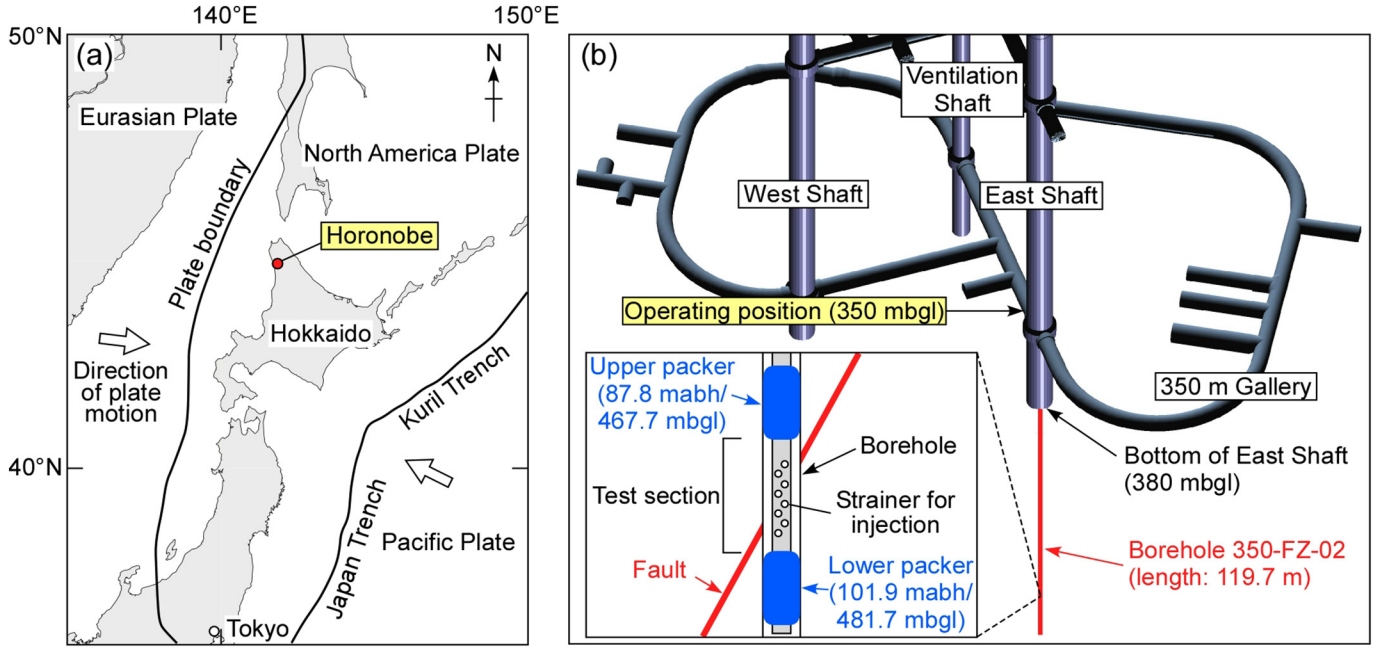

Fig. 1. (a) Location of the Horonobe area. (b) Layout of borehole 350-FZ-02 and the underground facility. Mabh = meters along borehole; mbgl = meters below ground level.

a borehole extensometer (Schweisinger et al., 2007), a borehole tiltmeter (Burbey et al., 2012), or a three-component borehole deformation sensor (Guglielmi et al., 2014).

This work reports the results of an injection test using a conventional straddle-sliding-packer system performed on a fault in Neogene siliceous mudstone from the Wakkanai Formation in the Horonobe area of Hokkaido, Japan (Fig. 1a). During testing, a new method was applied in which shear displacement along the fault during injection was monitored by measuring water pressure in the sliding packers. This method does not require specialized equipment and can be employed along with the usual hydraulic tests, as described below.

2. Materials

In the Horonobe area, borehole investigations and the construction of an underground facility have been ongoing since 2001 for research and development relevant to radioactive waste disposal. Consequently, conductive faults have been found within the Wakkanai Formation (Ishii, 2015; Ishii et al., 2011), although their hydraulic connectivity in the deeper parts of the formation (generally deeper than 400 m below ground level, mbgl) is limited (Ishii, 2018). The injection tests were performed on a fault (shear fracture) at 99.5 m along the borehole (mabh; 479.3 mbgl) in vertical borehole 350-FZ-02 (borehole length 119.7 m; drilling diameter 101 mm; drillcore diameter 63.5 mm) that was drilled from the bottom face (380 mbgl) of the East Shaft in the underground facility (Fig. 1b). This depth corresponds to the uppermost level of the lower Wakkanai Formation where the hydraulic connectivity of faults is limited (Ishii, 2018).

The host rock (siliceous mudstone) contains opal–cristobalite/tridymite (opal–CT) (40–45 wt%), clay (19–33 wt%), quartz (9–13 wt%), and feldspar (7–13 wt%) (Ishii et al., 2011). Its physical properties are as follows: tensile strength = 1.8 ± 0.7 MPa (± 1σ), unconfined compressive strength = 22.4 ± 5.4 MPa (± 1σ), Young's modulus = 1–5 GPa, Poisson's ratio = ~0.2, porosity = ~40%, and intrinsic permeability = 10^{-19} m^2 (Ishii et al., 2011; Miyazawa et al., 2011; Niunoya and Matsui, 2007). The fault at 99.5 mabh (479.3 mbgl) exhibits a dip direction/dip angle of 181°/71° (Fig. 2a), a thin layer of fault breccia (millimeters or less) (Fig. 2b, c), and striations (rake ≈ 90°) on the fault surface (Fig. 2d), although slickensteps are not clearly identified. A splay crack (hybrid fracture; Ishii, 2016) is also observed as a secondary fracture (Fig. 2a, c), which propagates at an angle of 30°–40° from the main fault surface (Fig. 2d). The orientations of the splay crack and striations on the fault surface indicate that the fault is a normal fault without a strike-slip component (Fig. 2d). Although the shear displacement of this fault is unknown, Ishii et al. (2010) reported the shear displacements of similar faults exposed on a surface outcrop to be up to 0.6 m (exceptionally ~10 m for a largest fault).

In situ stress measurements in boreholes (HDB-1, −3, and − 6) near the underground facility showed the far-field maximum principal stress to be oriented E–W and the stress regime to be generally characterized by reverse/strike-slip faulting (Fig. 3; Sanada et al., 2010, 2012). However, a normal faulting stress regime (E–W-directed horizontal maximum principal stress) was also observed within a range of decameters from the test section (HDB-6_416.0 m in Fig. 3), which is consistent with the sense of displacement of the fault (Fig. 2d). The pore pressure around the test section before excavation of the underground facility and subsequent pumping was ~4.9 MPa (Yoshino et al., 2015), but dehydration due to the pumping has reduced this to the current value of 3.9–4.5 MPa.

3. Methods

3.1. Injection

A constant-head step injection test was performed on the fault for two days (29 and 30 October 2018). The test used a conventional straddle-sliding-packer system and considered the section from 87.8 to 101.9 mabh (467.7–481.7 mbgl) (Fig. 1b). A plunger pump (plus an accumulator tank) was used for injection, and the water pressure in the test section (called “the test-section pressure”) was increased and decreased in steps of ~0.5 MPa while the test-section pressure was manually controlled by adjusting a regulating valve on the pump (i.e., adjusting the injection flow rate) at 350 mbgl (Fig. 1b). During each step, water injection was continued at a constant head until the flow rate was nearly stable. During pressure decrease steps, the test-section pressure was forcibly decreased by opening the regulating valve. At this time, back-flows occasionally occurred into the water tank at 350 mbgl. Stainless steel rods (outer diameter 41 mm; inner diameter 34 mm)

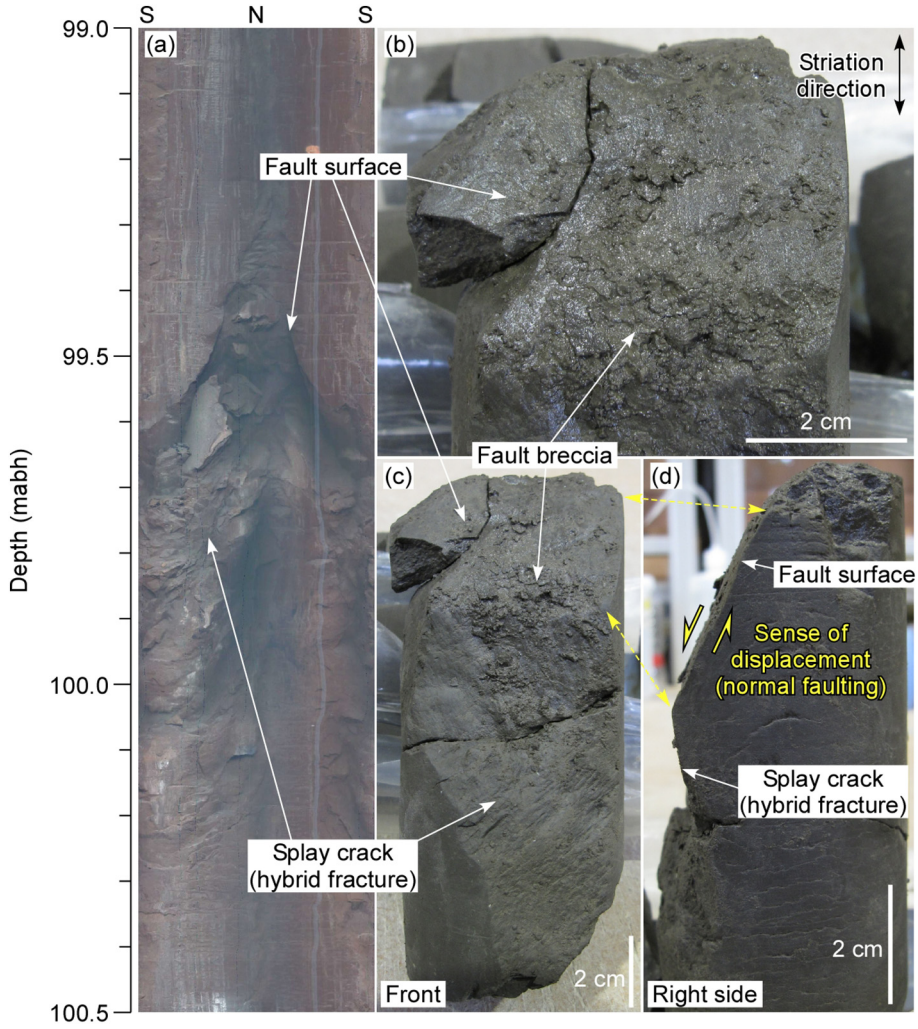

Fig. 2. (a) Image of borehole wall and (b–d) the drill core containing the injected fault in borehole 350-FZ-02.

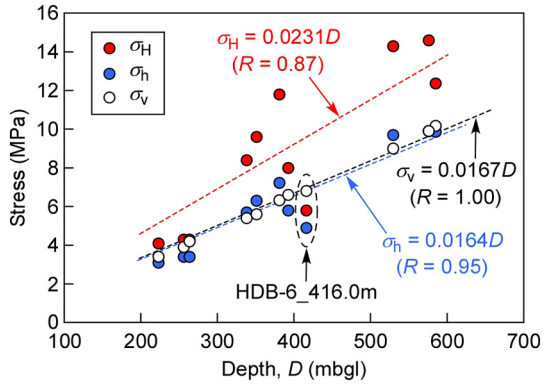

Fig. 3. Maximum and minimum horizontal stresses (σ_H and σ_h, respectively) measured by the hydraulic fracturing method, and the vertical (overburden) stress (σ_v) calculated using rock density in boreholes HDB-1, −3, and − 6 located near the underground facility (Sanada et al., 2010, 2012). The distance between the injected fault zone in 350-FZ-02 (−419.3 masl, meters above sea level) and the location of HDB-6_416.0 m (−355.8 masl) is 64 m.

with strainers (plus a pressure-resistance hose) were used as an injection line into the test section to reduce pressure loss during injection (Fig. 1b), and the injection flow rate was monitored by a mass flow meter installed on the downstream side of the pump at 350 mbgl. The test-section pressure, and the water pressures in the upper and lower packers (called “the upper-packer pressure” and “the lower-packer pressure”, respectively), were monitored by pressure sensors installed at 350 mbgl, connected by poly-ether-ether-ketone (PEEK) tubes (length 150 m). The recording interval was 1 s. After the 29th of October injection, the test section was shut in, and the test-section pressure recovered under natural conditions.

3.2. Function of the packer system

Sliding packers with a tube length of 0.9 m were used. The packers are inflated with water, and the bottom end slides as the packer tube expands, while the top end is fixed (Fig. 4a). When a sliding packer is inflated in a borehole and the top end is pulled upward, the packer tube is extended upward and the volume of the packer increases, reducing the packer pressure (Fig. 4b). Conversely, when the top end is pulled downward, the packer tube is shortened, the volume of the packer reduces, and its pressure increases (Fig. 4c). However, when the borehole wall is elastically soft, shortening the packer tube expands the borehole wall, and the packer pressure decreases. This is because the packer rubber contains steel wire fabric with a constant stiffness.

The displacement of the packer's top end (Δu_p, m, positive sign when the top end is pulled upward), the change in its pressure (Δp_p, Pa), and the axial force increment (ΔF, N, positive sign when the top end is pulled upward) can be related as follows:

$$\Delta F = a V_p c_p \Delta p_p, \tag{3}$$

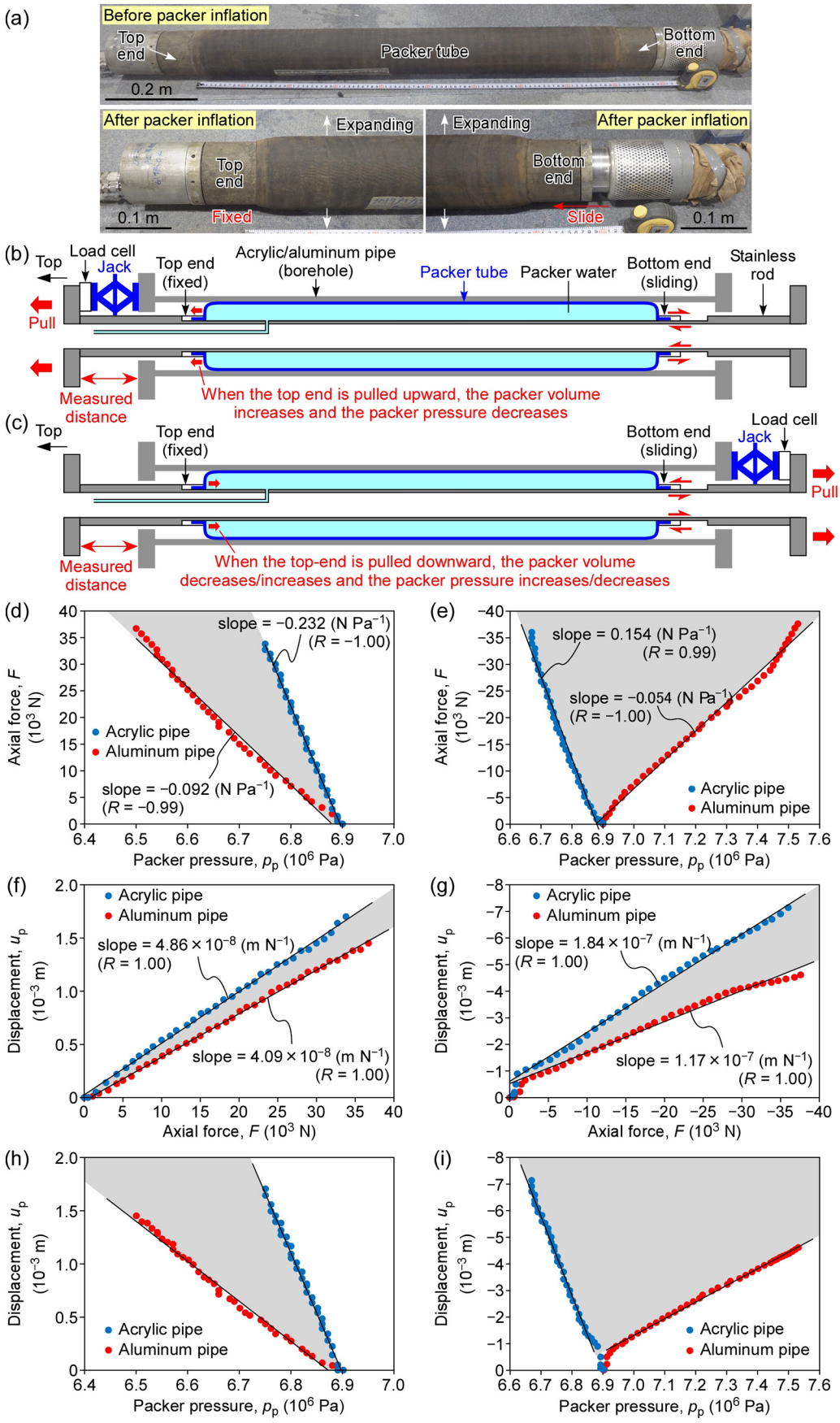

Fig. 4. (a) Photograph of a sliding packer. When the packer tube is inflated, the bottom end slides toward the top while the top end is fixed. (b, c) Schematic diagrams of the laboratory experiment for measuring u_p, p_p, and F when the top end is pulled (b) upward (to the borehole mouth) and (c) downward (toward the bottom). (d, e) Measured F and p_p during the experiment when the top end is pulled (d) upward and (e) downward. (f, g) Measured u_p and F during the experiment when the top end is pulled (f) upward and (g) downward. (h, i) Measured u_p and p_p during the experiment when the top end is pulled (h) upward and (i) downward. The regression lines are also shown in (d) to (i). These diagrams refer to both upper and lower packers.

$$\Delta u_p = b\Delta F, \quad (4)$$

where the coefficients a and b can be determined from a laboratory experiment (N m^{-3} and m N^{-1}, respectively), V_p is the volume of the packer plus PEEK tubes filled with packer water (m^3), and c_p is the compressibility of water (Pa^{-1}).

3.3. Laboratory experiment to determine coefficients a and b

During the laboratory experiment, the packer was inflated in pipes that have the same inner diameter as the borehole (~104.5 mm for the upper packer and ~ 103.9 mm for the lower packer, as measured by caliper logging) and the same elasticity as the borehole wall. Inflation continued until the packer pressure was similar to that used during the in situ injection test, and at that stage the top end of the packer was pulled to the top or to the bottom by a jack (Fig. 4b, c). Following this, the coefficients a and b were determined from the measured displacement of the top end, the change in packer pressure, and the axial force increment (Fig. 4b, c).

The pipes were selected based on the following equation derived from the theory of linear elasticity for isotropic media:

$$\Delta r_p/r_p = \Delta p_p(((r_p + t_p)^2 + r_p^2)/((r_p + t_p)^2 - r_p^2) + \nu_p)/E_p \quad (5)$$

where r_p is the pipe inner radius (m), Δr_p is the change of r_p (m), Δp_p is an increment of the packer pressure (Pa), and E_p, ν_p, and t_p are Young's modulus (Pa), Poisson's ratio, and thickness (m) of the pipe, respectively. Assuming infinite thickness for the borehole wall gives the following:

$$\Delta r_w/r_w = \Delta p_p(1 + \nu)/E \quad (6)$$

Here, r_w is for the borehole, and is 0.052 m; E and ν are for the borehole wall, and are 1–5 GPa and ~ 0.2, respectively, according to the results from previous laboratory tests and in situ pressuremeter tests (Miyazawa et al., 2011; Niunoya and Matsui, 2007). Generic acrylic pipe (E = 3.0 GPa, ν = 0.36, inner diameter 52.5 mm, thickness 10 mm) and generic aluminum pipe (E = 68.6 GPa, ν = 0.34, inner diameter 52.0 mm, thickness 3 mm) were selected based on Eqs. (5) and (6). They are equivalent to a borehole with walls having E = 0.6 and 4.5 GPa, respectively, assuming ν = 0.2. Thus, these pipes represent the possible upper and lower limits of the elastic stiffness of the borehole wall, and the effective coefficients a and b for the borehole wall are expected to be within the ranges of the coefficients for these model pipes.

Fig. 4d–i shows the results of the laboratory experiment; the values of aV_pc_p and b are -0.232 N Pa^{-1} and 4.86×10^{-8} m N^{-1} for the acrylic pipe and -0.092 N Pa^{-1} and 4.09×10^{-8} m N^{-1} for the aluminum pipe, respectively, when the top end is pulled upward (Fig. 4d, f). When the top end is pulled downward, these values are 0.154 N Pa^{-1} and 1.84×10^{-7} m N^{-1} for the acrylic pipe and -0.054 N Pa^{-1} and 1.17×10^{-7} m N^{-1} for the aluminum pipe, respectively (Fig. 4e, g). The coefficient a can be derived from these results using the known compressibility of water c_p and the volume of packer water V_p during the laboratory experiment (5×10^{-10} Pa^{-1} and 1.3×10^{-3} m^3, respectively). When the top end is pulled upward a is -3.56×10^{11} N m^{-3} for the acrylic pipe and -1.41×10^{11} N m^{-3} for the aluminum pipe. When the top end is pulled downward it is 2.36×10^{11} N m^{-3} for the acrylic pipe and -0.83×10^{11} N m^{-3} for the aluminum pipe. Although the displacement increased nonlinearly during the first axial force increment up to 1–2 kN when the top end was pulled downward (Fig. 4g), this initial increase was small enough to be ignored. As a result, the gray zones shown in Fig. 4d–i represent the possible ranges for the relationships between the displacement of the packer's top end, the change in packer pressure, and the axial force increment during the injection test.

3.4. Calculation of axial displacement of the test section during injection

The change in test-section length during injection (Δl, m) is defined as follows:

$$\Delta l = \Delta u_{pl} - \Delta u_{pu} \quad (7)$$

where Δu_{pu} and Δu_{pl} are the displacements of the upper and lower packers' top ends (m), respectively. The displacement of the top end of the packer that is pulled upward can be calculated from the change in its packer pressure and the coefficients a and b (i.e., the combinations of -3.56×10^{11} N m^{-3} and 4.86×10^{-8} m N^{-1} for the acrylic pipe and of -1.41×10^{11} N m^{-3} and 4.09×10^{-8} m N^{-1} for the aluminum pipe) (Fig. 4d, f). On the other hand, the displacement of the top end of the packer that is pulled downward cannot be determined from the change in its packer pressure. This is because the two empirical lines (i.e., the gray zone) shown in Fig. 4e do not provide constraints on axial force increments during changes in packer pressure. However, the displacement can be calculated from the change in packer pressure for the other packer whose top end is pulled upward, because the scalars of axial force increments imposed on the two top ends of the upper- and lower-packers during testing are always the same. Therefore, the used coefficients a and b are the combinations of -3.56×10^{11} N m^{-3} and 1.84×10^{-7} m N^{-1} for the acrylic pipe, and -1.41×10^{11} N m^{-3} and 1.17×10^{-7} m N^{-1} for the aluminum pipe (Fig. 4d, g). In summary, Δl (m) can be calculated from the following equation:

$$\Delta l = -a^*(b_u + b_l)V_pc_p\Delta p_p^* \quad (8)$$

where a^* is the coefficient for the packer whose top end is pulled upward (i.e., -3.56×10^{11} N m^{-3} for the acrylic pipe and -1.41×10^{11} N m^{-3} for the aluminum pipe), b_u and b_l are the coefficients for the upper and lower packers (m N^{-1}), respectively, ($b_u + b_l$) is 2.33×10^{-7} m N^{-1} for the acrylic pipe and 1.58×10^{-7} m N^{-1} for the aluminum pipe, V_p is the volume of packer water during the injection test (i.e., 3.2×10^{-3} m^3 considering the PEEK tubes of 150 m), c_p is the compressibility of water (i.e., 5×10^{-10} Pa^{-1}), and Δp_p^* is the change in packer pressure for the packer whose top end is pulled upward. The criteria for judging which packer's top end is pulled upward are summarized in Table 1.

As the packer pressure can also change during elastic expansion/contraction of the packer tube due to changes in test-section pressure, it is necessary to remove this effect by identifying the linear relationship between the packer pressure and test-section pressure during low-pressure phases of injection to the fault (or intact rock). Strain of the stainless steel rods is disregarded because steel is more resistant to strain than the packer.

Table 1
Criteria for assessing which packer's top end is pulled upward.

Upper-packer pressure (p_{pu})	Lower-packer pressure (p_{pl})	Test-section strain	Packer whose top end is pulled upward
Increase/no change	Decrease	Lengthen	Lower packer
Decrease	Increase/no change	Shorten	Upper packer
Decrease ($\Delta p_{pu}/\Delta p_{pl} > 1.5$)	Decrease	Shorten	Upper packer
Decrease ($\Delta p_{pu}/\Delta p_{pl} < 0.6$)	Decrease	Lengthen	Lower packer
Decrease ($0.6 \le \Delta p_{pu}/\Delta p_{pl} \le 1.5$)	Decrease	Lengthen/shorten	Upper/lower packer

3.5. Estimation of shear displacement along the fault during injection

Shear displacement along the fault during injection (Δu_s, m, positive sign when the sense of displacement is normal faulting) is defined by the following equation:

$$\Delta u_s = (\Delta\delta_m cos\theta - \Delta l)/sin\theta \quad (9)$$

where $\Delta\delta_m$ is the mechanical (or void) aperture increment of the fault (m), θ is the dip angle of the fault (i.e., 71°), and Δl is the change in test-section length (m) calculated from Eq. (8). This equation assumes a simple geometry, ignoring any tilt of the borehole during the test. In addition, the equation gives a minimum estimate of the possible shear displacement, because the strike-slip component cannot be measured by this method.

The mechanical aperture δ_m can be related to the hydraulic aperture δ_h by the following equation (Barton et al., 1985):

$$\delta_m = \sqrt{\delta_h JRC_0^{2.5}} \quad (10)$$

where JRC_0 is the joint roughness coefficient (JRC) on the laboratory scale. The units of δ_m and δ_h in this equation are microns, and this equation is only valid for $\delta_m \geq \delta_h$. When the δ_m value calculated from δ_h is smaller than the δ_h value, the δ_m value is assumed to be the same as the δ_h value (Barton, 1982). Although numerous correlations between δ_m and δ_h have been proposed (see reviews by Li et al., 2019; Shahbazi et al., 2020; Sun et al., 2020), Eq. (10) is one popular correlation (Li et al., 2014; Pan et al., 2010; Zhan et al., 2016).

The hydraulic aperture δ_h can be calculated from the transmissivity of the fault, based on Eq. (1). To estimate the transmissivity of the fault, the test-section pressure and injection flow rate were analyzed using well test analysis software (nSIGHTS, n-dimensional Statistical Inverse Graphical Hydraulic Test Simulator; Beauheim et al., 2014; Nuclear Waste Management Program, 2011). This program simulates a single-phase, one-dimensional radial/non-radial flow regime or a two-dimensional radial flow regime, with a borehole at the center of the modeled flow system. The present study determined the transmissivity of the test section for each injection step by fitting the measured and simulated flow rates, while the simulation considered entire injection sequences as the pressure history (Fig. 5). The fault was modeled as a 0.1 m thick, homogeneous, horizontal and infinite aquifer, where a transient, radial, and laminar flow was assumed. The fitting parameters were the fault transmissivity, fault storativity, static formation pressure, and test-section compressibility, and the last two parameters were given narrow fitting ranges near the best estimates based on measurement data as follows. The best estimate of the static formation pressure during each injection step was given as follows: (1) the mean test-section pressure and the mean injection flow rate during the last minute of each injection step were measured and plotted, (2) regression lines were derived from the intervals showing a linear relationship between the test-section pressure and injection flow rate, and (3) the pressure on the regression lines for zero injection flow rate was given as the best estimate of the static formation pressure during each step (cf., Huang et al., 2018). The best estimate of the test-section compressibility was 2.38×10^{-10} Pa^{-1} based on data from a pulse test.

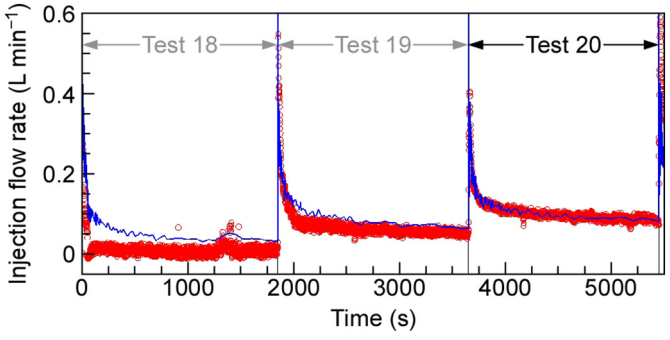

Fig. 5. Representative fitting analysis between measured (red) and simulated (blue) flow rates for each injection step. Test 20 is the given example. (For interpretation of the references to colour in this figure legend, the reader is referred to the web version of this article.)

The JRC_0 of the fault can be calculated based on the maximum height of the fracture-surface profile (R_z, mm; equal to the vertical distance between the highest peak and the lowest valley in the profile) (Li and Zhang, 2015). Although numerous methods for determining JRC_0 have been proposed, the method using R_z is simple and practical, and less sensitive to the problem of the sampling interval of data points (e.g., Bao et al., 2020; Liu et al., 2017; Zheng and Qi, 2016), according to Li and Zhang (2015). Four profiles parallel to the striations on the fault surface were traced using a profile gauge, which resulted in R_z of 0.3–0.7 mm. These values can be converted to a JRC_0 of 2–4 using the following empirical equation (Li and Zhang, 2015):

$$JRC_0 = 4.4192R_z^{0.6482} \quad (11)$$

In this study, the JRC_0 of the fault was assumed to be 3 (JRC_0 is commonly within 0–20 and higher JRC_0 indicates rougher surfaces).

3.6. Assessment of axial/normal compliance and normal stress

Assessing the compliance of equipment is important, as it may restrict the normal displacement of the fault. The axial compliance of equipment can be used as a measure of its compliance, and it should be greater than the normal compliance of the tested fault. From Eq. (4), the axial compliance C_a (m Pa^{-1}) of the packer system is given by the following equation:

$$C_a = (\Delta u_{pu} + \Delta u_{pl})r_w^2\pi/\Delta F = (b_u + b_l)r_w^2\pi \quad (12)$$

where Δu_{pu} and Δu_{pl} are the displacements of the upper and lower packers' top ends (m), respectively, r_w is the borehole radius (m), ΔF is the axial force increment (m), and b_u and b_l are the coefficients in Eq. (4) for the upper and lower packers (m N^{-1}), respectively. As $(b_u + b_l)$ is 1.58×10^{-7} m N^{-1} for the acrylic pipe and 2.33×10^{-7} m N^{-1} for the aluminum pipe (Fig. 4f, g), and r_w is 0.052 m, the axial compliance of the packer system is estimated to be between 1.3×10^{-9} and 2.0×10^{-9} m Pa^{-1}.

The normal compliance of the fault C_n (m Pa^{-1}) is defined as follows:

$$C_n = d\delta_m/d\sigma_n' \quad (13)$$

where δ_m is the mechanical fracture aperture (m) and σ'_n is the effective normal stress (Pa). The σ'_n is given as follows:

$$\sigma_n' = \sigma_n - \alpha p \quad (14)$$

where σ_n is the total normal stress (Pa), α is the effective stress coefficient (or Biot's coefficient), and p is the pore pressure (Pa). The coefficient α is assumed here to be 1, as usual for a fracture. The σ_n can be approximated to the test-section pressures below which the back-flows occurred during the pressure decrease steps after high-flow-rate injection (Rutqvist and Stephansson, 1996). This appoximation can be further optimized from the relationship between the test-section pressures p and the mechanical aperture δ_m during injection, as the effective normal stress σ'_n (Pa) and the mechanical aperture of a sheared fracture δ_m (m) can be expressed as the following semi-log relationship (Bandis et al., 1983):

$$\log_{10}\sigma_n' \propto q\delta_m \ (\sigma' n > 0) \quad (15)$$

where q is a coefficient (Pa m^{-1}). Parametric analysis of σ_n to minimize the negative correlation coefficient between $\log_{10}\sigma'_n$ and δ_m results in a regression line between $\log_{10}\sigma'_n$ and δ_m that gives the best estimates for σ_n and q. Using this result, Eq. (13) can be further developed to give the following equation (Bandis et al., 1983):

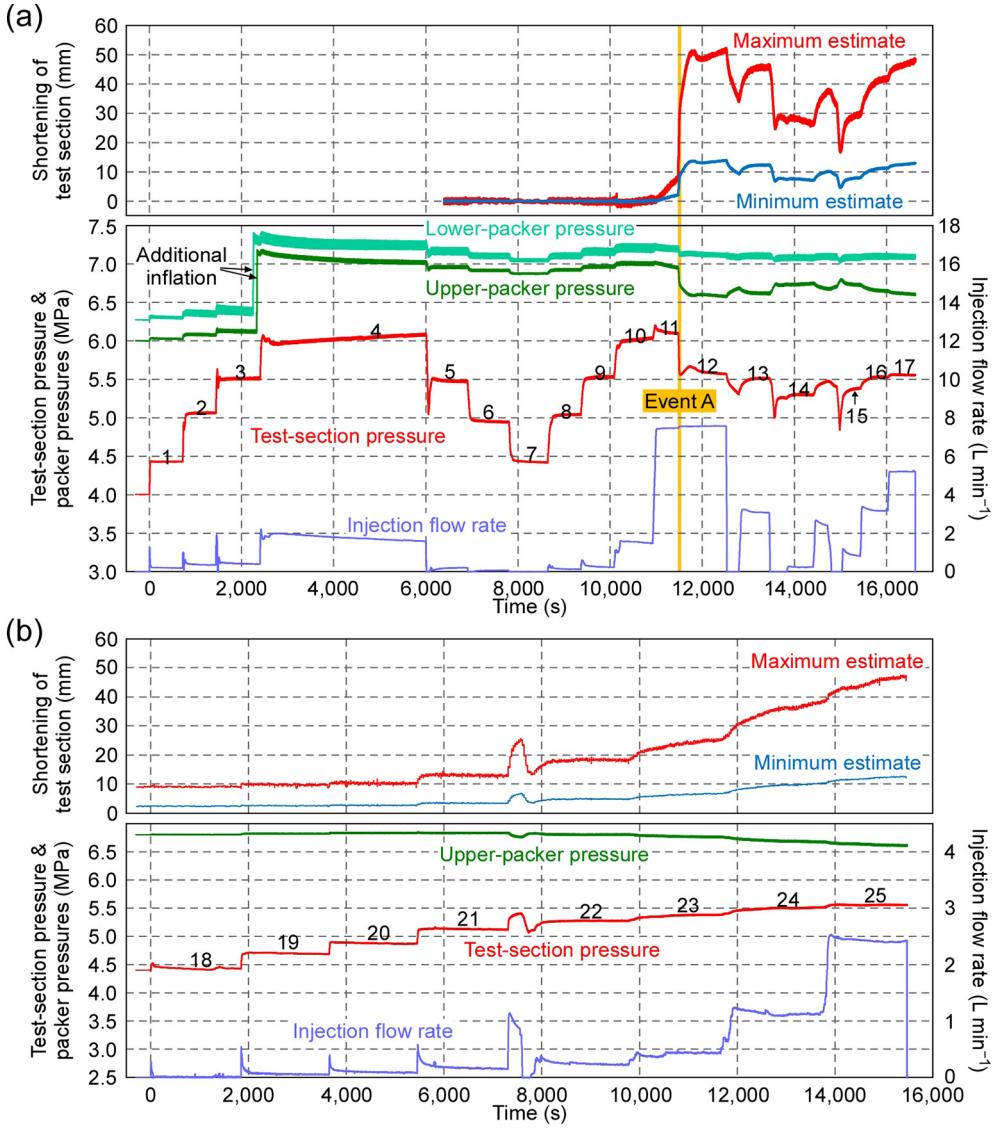

Fig. 6. Test-section pressure, packer pressures, injection flow rate, and shortening of the test section during injection tests performed on (a) 29th October 2018 and (b) 30th October 2018. The numbers (1 to 25) in the graphs refer to the test numbers of constant-head injection tests. A sudden pressure drop in the test section occurred between 11,478–11,500 s after the start of injection (labeled “event A" in the figure).

$$C_n = d\delta_m/d\sigma'_n = \log_{10} e/(q\sigma'_n) = 0.4343/(q\sigma'_n) \quad (16)$$

Note that this model assumes normal displacement upon fractures that occurs as a result of changes in effective normal stress, regardless of shear-induced dilation. As the effective change in fracture aperture during injection tests may also include a component of shear-induced dilation (Hsiung et al., 2005; Lei et al., 2016; Rinaldi and Rutqvist, 2019), the normal compliance derived from Eq. (16) may overestimate the normal compliance of the fault. However, the estimated σ_n is reliable, as the σ'_n at which the mechanical aperture asymptotically increases according to Eq. (15) is largely insensitive to the component of shear-induced dilation.

4. Results

4.1. Test-section pressure and injection flow rate

The changes in test-section pressure and injection flow rate during injection are summarized as follows. Although the flow rate increased linearly from 0 to 397 mL min^{-1}, and the test-section pressure increased from 3.9 to 5.5 MPa (tests 1–3 in Figs. 6a and 7a), the flow rate increased non-linearly when the test-section pressure increased to 6.0 MPa, and the flow rate was 1584 mL min^{-1} when the test-section pressure was 6.1 MPa (test 4 in Figs. 6a and 7a). Then, as the test-section pressure decreased and increased, the test-section pressure and the flow rate again changed linearly (tests 5–9 in Figs. 6a and 7b) (the back-flow occurred when the test-section pressure decreased to 6.04 MPa after test 4). The flow rate again increased non-linearly when the test-section pressure increased to 6.0 MPa, increasing the flow rate from 238 to 1479 mL min^{-1} (test 10 in Figs. 6a and 7b). Further increasing the test-section pressure to ≥6.1 MPa further increased the flow rate (7473 mL min^{-1}: test 11 in Figs. 6a and 7b). As injection continued, the test-section pressure suddenly dropped by 0.5 MPa (from 6.09 to 5.61 MPa) during a period of 22 s (event A in Fig. 6a) without a significant change in the flow rate (Fig. 6a). Then, the test-section pressure stabilized at ~5.6 MPa after some fluctuations (test 12 in Fig. 6a), and the flow rate varied non-linearly (tests 12–17 in Figs. 6a and 7c) (after tests 12 and 13, the back-flows occurred when the test-section pressure decreased to 5.52 MPa and 5.51 MPa, respectively). After test 17, the test section was shut in, and its pressure recovered under natural conditions. The next day, reinjection into the test section showed the same results as those of the previous day; that is, the flow

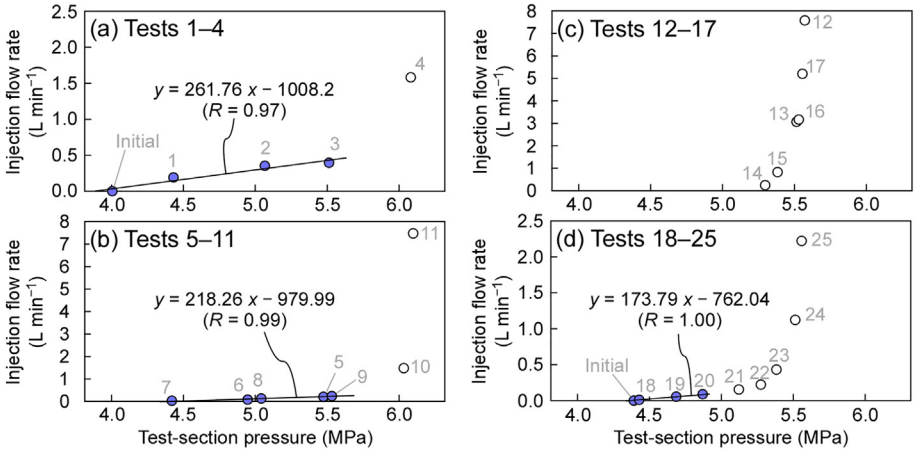

Fig. 7. Injection flow rate vs. test-section pressure determined by constant-head injection tests for tests (a) 1–4, (b) 5–11, (c) 12–17, and (d) 18–25. Solid circles denote data used to determine the regression lines for deriving the static formation pressure during each step. Each gray number indicates the constant-head injection test number.

rate increased linearly with test-section pressure up to 4.9 MPa (tests 18–20 in Figs. 6b and 7d), and then increased non-linearly when the test-section pressure was ≥5.3 MPa (tests 22–25 in Figs. 6a and 7b) (the back-flow occurred when the test-section pressure decreased to 5.55 MPa after test 25).

4.2. Packer pressures and axial strain of the test section

Injection caused changes in the upper-packer pressure. Here, changes are described only after test 5, because the change in packer pressure during the early phase of the test was mainly affected by the additional inflation performed from 2300 s after the start (Fig. 6a). When the test-section pressure was ≤6.0 MPa, the packer pressure changed linearly with varying test-section pressure on account of the elastic response (tests 5–10 in Figs. 6a and 8a). At this time, the elastic relationship between the packer pressure and test-section pressure was as follows (Fig. 8a):

$$p_p = 0.0815p + 6.5145 \times 10^6 \quad (17)$$

where p_p and p are the packer pressure (Pa) and test-section pressure (Pa), respectively. When the test-section pressure increased to ≥6.0 MPa, the packer pressure decreased. After the packer pressure decreased by 0.06 MPa during test 11, it suddenly dropped by 0.19 MPa during event A (Figs. 6a and 8a). It then slowly decreased by 0.18 MPa and stabilized at 6.6 MPa with no significant change in the test-section pressure during test 12 (Figs. 6a and 8a). After that, when the test-section pressure was approximately > 5.0 MPa, the packer pressure began to change inversely with the test-section pressure during tests 13–25 (Figs. 6 and 8a, b).

For the lower-packer pressure, an elastic response was observed following changes in the test-section pressure, similar to the upper-packer pressure (Figs. 6a and 8c). However, it did not show the remarkable changes as observed in the upper-packer pressure after test 11 (Figs. 6a and 8c). After test 17, the lower-packer pressure decreased significantly owing to a leak from a connector in the PEEK tubes (Fig. 8c). This leak might have started to occur intermittently during injection and could have decreased the lower-packer pressure slightly, as a slight decrease was observed with time (Fig. 8c). During tests 18–25, the lower packer was inflated only to maintain hydraulic isolation of the test section. Its pressure during these tests is therefore not shown in Fig. 6b.

The upper-packer pressure significantly decreased, while the lower-packer pressure remained almost constant, except for the elastic response following changes in the test-section pressure (Fig. 8). Such changes in packer pressures indicate that the test section shortened and the upper packer's top end was pulled upward during the test (Table 1). By removing the elastic component due to the change in the test-section pressure using Eqs. (17), (8) can be expressed as follows:

$$\Delta l = -a_u(b_u + b_l)V_p c_p[p_{pu} - (0.0815p + 6.6514 \times 10^6)] \quad (18)$$

where a_u is the coefficient in Eq. (3) for the upper packer (i.e., -3.56×10^{11} N m^{-3} from the acrylic pipe and -1.41×10^{11} N m^{-3} from the aluminum pipe), b_u and b_l are the coefficients in Eq. (4) for the upper and lower packers, respectively (i.e., $b_u + b_l = 1.58 \times 10^{-7}$ m N^{-1} from the acrylic pipe and 2.33×10^{-7} m N^{-1} from the aluminum pipe), V_p is the volume of packer water during the in situ injection test (i.e., 3.2×10^{-3} m^3), c_p is the compressibility of water (i.e., 5×10^{-10} Pa^{-1}), p_{pu} is the upper-packer pressure (Pa), and p is the test-section pressure (Pa).

Fig. 6 shows the calculated shortening of the test section, where the maximum estimate represents the values calculated using the coefficients a and b for the acrylic pipe, while the minimum estimate gives the values calculated using the coefficients for the aluminum pipe. This shortening can be attributed to shear movement along the fault by normal faulting, as other factors cannot be considered.

4.3. Hydraulic aperture increment of the fault

The best estimate of the static formation pressure at each injection step is 3.85 MPa for tests 1–4, 4.49 MPa for tests 5–11, and 4.38 MPa for tests 18–25, based on the regression lines in Fig. 7. For tests 12–17, a pressure of 4.38 MPa based on tests 18–25 was assigned because no linear relationship between the test-section pressures and injection flow rates was identified from tests 12–17 (Fig. 7c). According to these assumed static formation pressures, the transmissivities of the test section for tests 1–4, 8–11, and 18–25 were estimated as shown in Fig. 9a (pressure-decrease steps in tests 5–7 were not calculated, considering the back-flows observed during the tests). Furthermore, applying Eq. (1) to those transmissivities, the hydraulic apertures of the fault at different test-section pressures were calculated as shown in Fig. 9b. Results are as follows:

- A significant increase in hydraulic aperture was observed at high test-section pressure (Fig. 9b).
- The test-section pressure at which the hydraulic aperture asymptotically increases was ~6.1 MPa before event A and ~ 5.6 MPa after event A (Fig. 9b).
- The hydraulic apertures at low test-section pressures before and after event A are similar (Fig. 9b).

4.4. Shear displacement along the fault

For tests 8–25 where the packer pressures and the hydraulic apertures were evaluated, the total shear displacement of the fault during

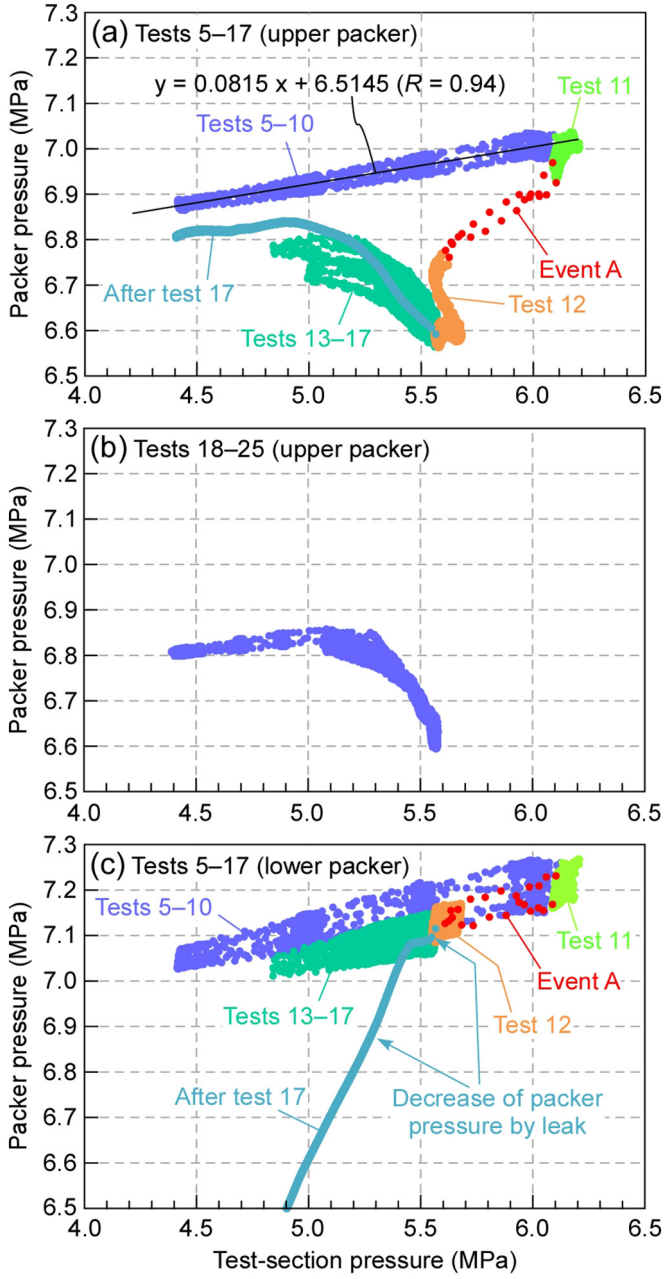

Fig. 8. Packer pressure vs. test-section pressure during the injection tests. Upper-packer pressure during (a) tests 5–17 and (b) tests 18–25, and (c) lower-packer pressure during tests 5–17. The regression line in (a) was obtained from 6400 to 10,237 s during tests 5–10.

the last 10 s of each injection step (Δu_s, m) was calculated by Eq. (9). The mechanical aperture δ_m of the fault was calculated by applying Eq. (10) (all δ_m were assumed to be equal to δ_h because all the δ_m calculated from δ_h were smaller than the δ_h). The calculated total shear displacement is plotted in Fig. 9c. The main results concerning the shear displacement are as follows:

- The calculated total shear displacement has a maximum of 13.3–49.5 mm (Fig. 9c).
- The total shear displacements at low test-section pressures after event A confirmed a residual shear displacement of 2.8–10.4 mm after event A (Fig. 9c).
- The onset of shearing occurred at a test-section pressure of ~6.0 MPa before event A, while after event A the onset occurred at a test-section pressure of ~4.7 MPa (Fig. 9c).

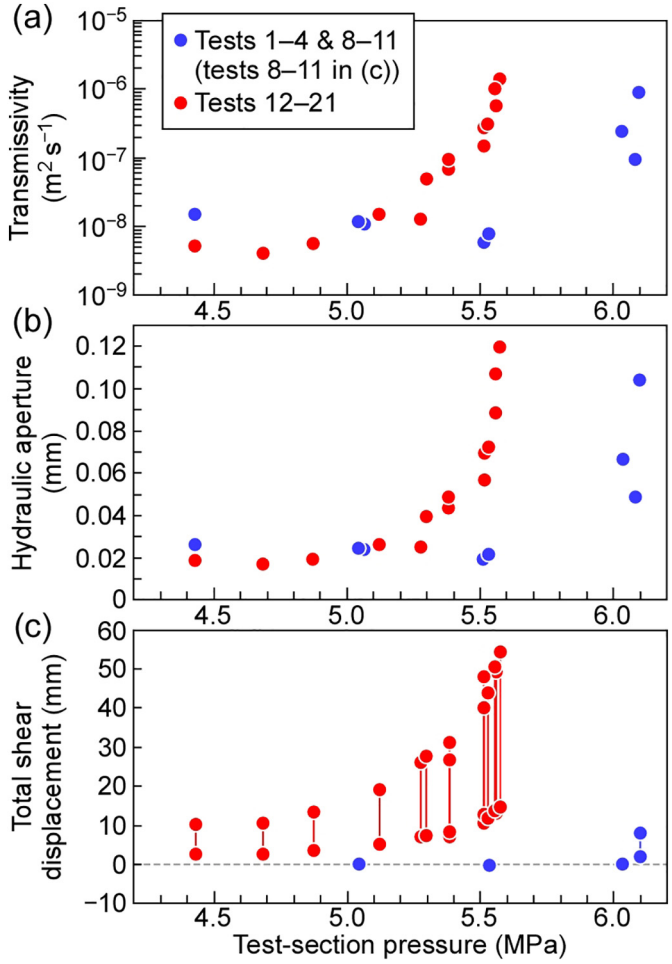

Fig. 9. (a) Transmissivity, (b) hydraulic aperture, and (c) total shear displacement of the fault with respect to test-section pressure.

4.5. Normal compliance and normal stress

The relationship between fault displacement and test-section pressure was different before and after event A (section 4.3 and 4.4); the test-section pressure at which the hydraulic aperture asymptotically increases decreased after event A (Fig. 9b), and the test-section pressure at which the onset of shearing occurs also decreased after event A (Fig. 9c). This observation indicates a possibility that normal and shear stiffnesses of the fault both decreased after event A, indicating that a loss of cohesion occurred at cohesive asperities (e.g., healed part) within the fault through event A (cf., the break-up of a fracture: Rutqvist, 2015; Rutqvist and Stephansson, 1996). Given the possibility that the fault was partly cohesive before event A, the back-flow method described in section 3.6 and the empirical method using Eqs. (15) and (16) might not be valid to estimating the normal stress acting across the fault before event A, as those methods basically assume a cohesionless fracture. Therefore, this study estimated only the normal stress and normal compliance of the fault after event A as below.

After tests 12, 13, and 25, the back-flows occurred when the test-section pressure decreased to 5.51, 5.52, and 5.55 MPa, respectively (section 4.1). These pressures are very close to each other and are inferred to represent the normal stress across the fault. For each pressure, the regression line was derived as shown in Fig. 10a by applying Eqs. (14) and (15) to the mechanical aperture δ_m and test-section pressure p, which resulted in the best estimate of 5.55 MPa for σ_n to minimize the

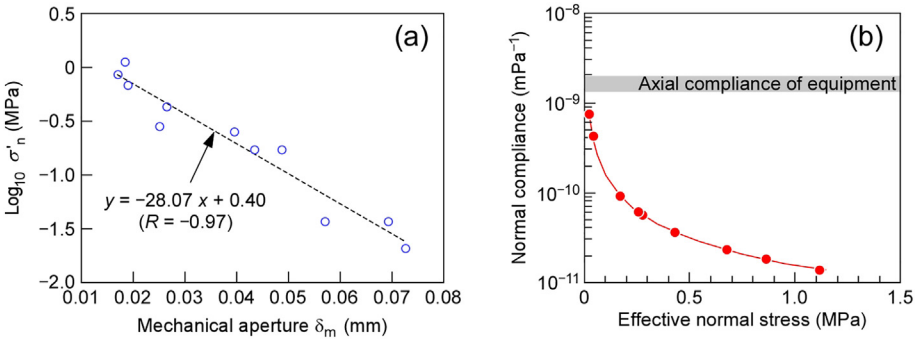

Fig. 10. (a) Regression line between $\log_{10}\sigma'_n$ and δ_m for tests 13–24 (excluding test 17) after event A when σ_n is 5.55 MPa and (b) the estimated normal compliance of the fault with respect to the estimated effective normal stress.

negative correlation coefficient between $\log_{10}\sigma'_n$ and δ_m (the correlation coefficients were − 0.91, −0.96, and − 0.97 for σ_n of 5.51, 5.52, and 5.55 MPa, respectively). From the slope of the regression line at σ_n = 5.55 MPa (Fig. 10a) and Eqs. (15) and (16), the normal compliance of the fault after event A was estimated as shown in Fig. 10b and was found to be significantly smaller than the axial compliance of the packer system.

5. Discussion

5.1. Reliability of shear displacements estimated using the applied packer method

The lower-packer pressure did not change significantly during the test, except for the elastic response following changes in test-section pressure (Figs. 6 and 8c). This observation is compatible with results from the laboratory experiment (Table 1) showing that one packer may remain constant while the pressure in the other packer decreases (as shown by the gray zones in Fig. 4h, i). Furthermore, the estimated shortening of the test section reflects shear movement along the fault in the sense of normal faulting (section 4.2), which is consistent with the previous displacement interpreted from observations of drill cores (Fig. 2d).

The estimated shear displacement (Fig. 9c) is considered reliable because the measured and empirically predicted shear stiffnesses of the fault (K_s, Pa m^{-1}) are consistent, as described further below. The measured K_s during tests 18–24 (i.e., the pressure-increase step when the test-section pressure was less than the total normal stress across the fault on 30th October 2018) can be defined as follows (Guglielmi et al., 2014):

$$K_s = \Delta\tau/\Delta u_s \tag{19}$$

$$\Delta\tau = \Delta p^* \tan\phi \tag{20}$$

where $\Delta\tau$, Δu_s, and Δp^* are the excess-shear-stress increment (Pa), shear-displacement increment (m), and pressure increment (Pa), respectively, and ϕ is the friction angle of the fault (°). Here, those increments are defined as the increments from test 18 to test 24. The ϕ can be estimated by the following equation (Barton et al., 1985):

$$\phi = JRC\log_{10}(JCS/\sigma'_n) + \phi_r \tag{21}$$

where JRC and JCS are, respectively, the joint roughness coefficient and joint wall compressive strength (Pa) at an in situ scale, and ϕ_r is the residual friction angle (°). The JRC and JCS can be related to values at a laboratory scale using the following equations (Barton et al., 1985):

$$JRC = JRC_0(L/0.1)^{-0.02JRC_0} \tag{22}$$

$$JCS = JCS_0(L/0.1)^{-0.03JRC_0} \tag{23}$$

where L is the length of the fracture (m), and JRC_0 and JCS_0 are those values for L = 0.1 m. For unweathered fractures, JCS_0 and ϕ_r are equal to the unconfined compressive strength of the intact rock (UCS) and the basic friction angle ϕ_b, respectively, and ϕ_b can be obtained from tilt tests performed on samples with saw-cut surfaces (Barton and Choubey, 1977). Adopting the following parameters: ϕ_b = ~26° (results from the tilt tests); L = 0.1–10.0 m (assumption); JRC_0 = 3 (section 3.5); and UCS = 22.4 MPa (section 2), and by approximating the friction angle ϕ to be 32° based on Eqs. (21)–(23), the measured K_s during tests 18–24 is calculated to be 2.3 × 10^7 to 8.4 × 10^7 Pa m^{-1} using Eqs. (19)–(20).

The empirically predicted K_s during tests 18–24 is defined as follows (Barton and Choubey, 1977):

$$K_s = 1/u_{sp}\sigma'_n\tan(JRC\log_{10}(JCS/\sigma'_n) + \phi_r) \tag{24}$$

where u_{sp} is the shear displacement required to reach the peak shear strength (m). The u_{sp} can be derived from the following empirical equation suggested by Asadollahi and Tonon (2010):

$$u_{sp} = 0.0077L^{0.45}(\sigma'_n/JCS)^{0.34}\cos(JRC\log_{10}(JCS/\sigma'_n)). \tag{25}$$

By using Eqs. (24) and (25) with the effective normal stress at test 24, the empirically predicted K_s is calculated to be 0.8 × 10^7 to 7.1 × 10^7 Pa m^{-1}, which is comparable to the measured K_s. The clearance of ≥32 mm between the test rod and borehole wall in the test section (as measured by caliper logging; the borehole diameter is mostly ~104 mm in the test section but is enlarged up to ~124 mm near the fault due to the fault damage) is also sufficient to accommodate relatively large shear displacements during normal faulting at a dip angle of 71° (the maximum possible accommodation is ≥98 mm). Therefore, the estimated shear displacement is considered to be reliable. The estimated maximum shear displacement of 13.3–49.5 mm (Fig. 9c) is very large and comparable to the maximum of previously reported values (centimeters or less) for injection tests in other fields (De Barros et al., 2016; Derode et al., 2013; Evans et al., 2005; Guglielmi et al., 2015a, 2015b, 2017; Jeanne et al., 2018).

5.2. Applicability of the packer-pressure-based extensometer

This study has developed and demonstrated a new method for monitoring axial displacements of isolated test sections in a borehole during injection by utilizing sliding-packer pressures. However, the method has some disadvantages that are outlined below.

- The estimation error is large, as shown in Fig. 6.
- Whether the test section lengthens or shortens cannot be determined by changes in packer pressure when the upper and lower packer-pressures both decrease by similar amounts (e.g., the case of $0.6 \le \Delta p_{pu}/\Delta p_{pl} \le 1.5$ in Table 1 for this study).
- When the normal compliance of the fault is comparable to the axial compliance of the packer system (~2 × 10^{-9} m Pa^{-1} in this study), the equipment may restrict normal displacement on the fault. Normal compliance of fractures is commonly ~1 × 10^{-12} to ~1 × 10^{-9} m Pa^{-1}, based on previous field investigations (Burbey

et al., 2012; Cappa et al., 2006; Guglielmi et al., 2015b; Jeanne et al., 2018; Murdoch et al., 2009; Rutqvist et al., 1998; Schweisinger et al., 2009, 2011; Svenson et al., 2007, 2008). Due to the potential similarity between the normal compliance of fractures and the axial compliance of the packer, it is necessary to carefully check the compliances of the testing equipment and the fault, as shown in Fig. 10b.

Despite these disadvantages, this method does not need specialized equipment and can be conducted along with standard hydraulic tests. A sliding packer is a commonly available item, and the length of the test section is not restricted (14.1 m in this study). These advantages in the method's application may offset the disadvantages described above.

5.3. Implications for the hydraulic dilation angle of the fault

The hydraulic dilation angle of the fault can be estimated as follows. A residual shear displacement of 2.8–10.4 mm was observed after event A (Fig. 9c). However, the hydraulic aperture showed no significant change as a result of that displacement (Fig. 9b). Therefore, the hydraulic dilation angle of the fault is estimated to be effectively zero. The increments of hydraulic aperture observed at high test-section pressures are interpreted to be due to normal displacement of fractures caused by pore-pressure increase, regardless of shear-induced dilation (e.g., Rutqvist and Stephansson, 1996).

6. Summary

- A constant-head step injection test using a conventional straddle-packer system was performed on a normal fault (shear fracture) in siliceous mudstone.
- The tests applied a new method whereby axial displacements of isolated test sections in a borehole during injection are calculated from the pressures of sliding packers and the pore pressure in the test section, calibrated using a simple laboratory experiment.
- The hydraulic aperture, shear displacement, normal compliance, normal stress, and shear stiffness of the fault during the test were estimated using the new method.
- The hydraulic dilation angle is inferred to have been effectively zero, because the residual shear displacement observed after event A did not result in any increase in hydraulic aperture.
- The method developed and applied here does not require specialized equipment and is expected to aid investigation of the hydromechanical behavior of fractures or aquifers.

Declaration of Competing Interest

The authors declare that they have no known competing financial interests or personal relationships that could have appeared to influence the work reported in this paper.

Acknowledgments

The author thanks engineers of the Taisei Corporation, Asano Taiseikiso Engineering, and Mitsubishi Materials Techno Corporation for the borehole investigation, and Yoichi Samata, Nobukatsu Miyara, and Akitaka Sakurai of JAEA for performing the laboratory experiment. The author also thanks Larry Murdoch for valuable comments on the new packer method, an anonymous reviewer for insightful and detailed review, and Janusz Wasowski for editorial handling of the manuscript.

References

Asadollahi, P., Tonon, F., 2010. Constitutive model for rock fractures: revisiting Barton's empirical model. Eng. Geol. 113, 11–32.
Bandis, S.C., Lumsden, A.C., Barton, N.R., 1983. Fundamentals of rock joint deformation. Int. J. Rock Mech. Min. Sci. Geomech. Abstr. 20, 249–268.
Bao, H., Zhang, G., Lan, H., Yan, C., Xu, J., Xu, W., 2020. Geometrical heterogeneity of the joint roughness coefficient revealed by 3D laser scanning. Eng. Geol. 265, 105415.
Barton, N., 1982. Modelling Rock Joint Behaviour from In Situ Block Tests: Implications for Nuclear Waste Repository Design. ONWI-308. Office of Nuclear Waste Isolation, Columbus, OH.
Barton, N., Choubey, V., 1977. The shear strength of rock joints in theory and practice. Rock Mech. 10, 1–54.
Barton, N., Bandis, S., Bakhtar, K., 1985. Strength, deformation and conductivity coupling of rock joints. Int. J. Rock Mech. Min. Sci. Geomech. Abstr. 22, 121–140.
Beauheim, R.L., Roberts, R.M., Avis, J.D., 2014. Hydraulic testing of low-permeability Silurian and Ordovician strata, Michigan Basin, southwestern Ontario. J. Hydrol. 509, 163–178.
Birkholzera, J.T., Tsang, C.-F., Bond, A.E., Hudsond, J.A., Jing, L., Stephansson, O., 2019. 25 years of DECOVALEX - Scientific advances and lessons learned from an international research collaboration in coupled subsurface processes. Int. J. Rock Mech. Min. Sci. 122, 103995.
Burbey, T.J., Hisz, D., Murdoch, L.C., Zhang, M., 2012. Quantifying fractured crystalline-rock properties using well tests, earth tides and barometric effects. J. Hydrol. 414–415, 317–328.
Cappa, F., Guglielmi, Y., Rutqvist, J., Tsang, C.-F., Thoraval, A., 2006. Hydromechanical modelling of pulse tests that measure fluid pressure and fracture normal displacement at the Coaraze Laboratory site, France. Int. J. Rock Mech. Min. Sci. 43, 1062–1082.
Davies, R., Foulger, G., Bindley, A., Styles, P., 2013. Induced seismicity and hydraulic fracturing for the recovery of hydrocarbons. Mar. Pet. Geol. 45, 171–185.
De Barros, L., Daniel, G., Guglielmi, Y., Rivet, D., Caron, H., Payre, X., Bergery, G., Henry, P., Castilla, R., Dick, P., Barbieri, E., Gourlay, M., 2016. Fault structure, stress, or pressure control of the seismicity in shale? Insights from a controlled experiment of fluid-induced fault reactivation. J. Geophys. Res. Solid Earth 121, 4506–4522.
Dempsey, D., Kelkar, S., Davatzes, N., Hickman, S., Moos, D., 2015. Numerical modeling of injection, stress and permeability enhancement during shear stimulation at the Desert Peak Enhanced Geothermal System. Int. J. Rock Mech. Min. Sci. 78, 190–206.
Derode, B., Cappa, F., Guglielmi, Y., Rutqvist, J., 2013. Coupled seismo-hydromechanical monitoring of inelastic effects on injection-induced fracture permeability. Int. J. Rock Mech. Min. Sci. 61, 266–274.
Ellsworth, W.L., 2013. Injection-induced earthquakes. Science 341. https://doi.org/10.1126/science.1225942.
Evans, K.F., Genter, A., Sausse, J., 2005. Permeability creation and damage due to massive fluid injections into granite at 3.5 km at Soultz: 1. Borehole observations. J. Geophys. Res. 110, B04203. https://doi.org/10.1029/2004JB003168.
Guglielmi, Y., Cappa, F., Lançon, H., Janowczyk, J.B., Rutqvist, J., Tsang, C.F., Wang, J.S.Y., 2014. ISRM suggested method for step-rate injection method for fracture in-situ properties (SIMFIP): using a 3-components borehole deformation sensor. Rock Mech. Rock. Eng. 47, 303–311.
Guglielmi, Y., Cappa, F., Avouac, J.-P., Henry, P., Elsworth, D., 2015a. Seismicity triggered by fluid injection–induced aseismic slip. Science 348, 1224–1226.
Guglielmi, Y., Elsworth, D., Cappa, F., Henry, P., Gout, C., Dick, P., Durand, J., 2015b. In situ observations on the coupling between hydraulic diffusivity and displacements during fault reactivation in shales. J. Geophys. Res. Solid Earth 120, 7729–7748.
Guglielmi, Y., Birkholzer, J., Rutqvist, J., Jeanne, P., Nussbaum, C., 2017. Can fault leakage occur before or without reactivation? Results from an in situ fault reactivation experiment at Mont Terri. Energy Procedia 114, 3167–3174.
Guglielmi, Y., Nussbaum, C., Jeanne, P., Rutqvist, J., Cappa, F., Birkholzer, J., 2020. Complexity of fault rupture and fluid leakage in shale: Insights from a controlled fault activation experiment. J. Geophys. Res. Solid Earth 125, e2019JB017781.
Healy, J.H., Rubey, W.W., Griggs, D.T., Raleigh, C.B., 1966. The Denver Earthquakes. Science 161, 1301–1310.
Hsieh, P.A., Bredehoeft, J.D., 1981. A reservoir analysis of the Denver Earthquakes: a case of induced seismicity. J. Geophys. Res. 86, 903–920.
Hsiung, S.M., Chowdhury, A.H., Nataraja, M.S., 2005. Numerical simulation of thermal–mechanical processes observed at the Drift-Scale Heater Test at Yucca Mountain, Nevada, USA. Int. J. Rock Mech. Min. Sci. 42, 652–666.
Huang, Z., Li, X., Li, S., Zhao, K., Zhang, R., 2018. Investigation of the hydraulic properties of deep fractured rocks around underground excavations using high-pressure injection tests. Eng. Geol. 245, 180–191.
Ishii, E., 2015. Predictions of the highest potential transmissivity of fractures in fault zones from rock rheology: preliminary results. J. Geophys. Res. Solid Earth 120, 2220–2241.
Ishii, E., 2016. Far-field stress dependency of the failure mode of damage-zone fractures in fault zones: results from laboratory tests and field observations of siliceous mudstone. J. Geophys. Res. Solid Earth 121, 70–91.
Ishii, E., 2018. Assessment of hydraulic connectivity of fractures in mudstones by single-borehole investigations. Water Resour. Res. 54, 3335–3356.
Ishii, E., Funaki, H., Tokiwa, T., Ota, K., 2010. Relationship between fault growth mechanism and permeability variations with depth of siliceous mudstones in northern Hokkaido, Japan. J. Struct. Geol. 32, 1792–1805.
Ishii, E., Sanada, H., Funaki, H., Sugita, Y., Kurikami, H., 2011. The relationships among brittleness, deformation behavior, and transport properties in mudstones: an example from the Horonobe Underground Research Laboratory, Japan. J. Geophys. Res. 116, B09206. https://doi.org/10.1029/2011JB008279.
Jeanne, P., Guglielmi, Y., Rutqvist, J., Nussbaum, C., Birkholzer, J., 2018. Permeability variations associated with fault reactivation in a claystone formation investigated by field experiments and numerical simulations. J. Geophys. Res. Solid Earth 123, 1694–1710.
Lei, Q., Latham, J.-P., Xiang, J., 2016. Implementation of an empirical joint constitutive model into finite-discrete element analysis of the geomechanical behaviour of

fractured rocks. Rock Mech. Rock. Eng. 49, 4799–4816.
Li, Y., Zhang, Y., 2015. Quantitative estimation of joint roughness coefficient using statistical parameters. Int. J. Rock Mech. Min. Sci. 77, 27–35.
Li, Y., Chen, Y.-F., Zhou, C.-B., 2014. Hydraulic properties of partially saturated rock fractures subjected to mechanical loading. Eng. Geol. 179, 24–31.
Li, B., Li, Y., Zhao, Z., Liu, R., 2019. A mechanical-hydraulic-solute transport model for rough-walled rock fractures subjected to shear under constant normal stiffness conditions. Journal of Hydrology 579.
Liu, X.G., Zhu, W.C., Yu, Q.L., Chen, S.J., Li, R.F., 2017. Estimation of the joint roughness coefficient of rock joints by consideration of two-order asperity and its application in double-joint shear tests. Eng. Geol. 220, 243–255.
McClure, M.W., Horne, R.N., 2014a. An investigation of stimulation mechanisms in Enhanced Geothermal Systems. Int. J. Rock Mech. Min. Sci. 72, 242–260.
McClure, M.W., Horne, R.N., 2014b. Correlations between formation properties and induced seismicity during high pressure injection into granitic rock. Eng. Geol. 175, 74–80.
Miyazawa, D., Sanada, H., Kiyama, T., Sugita, Y., Ishijima, Y., 2011. Poroelastic coefficients for siliceous rocks distributed in the Horonobe area, Hokkaido, Japan. J. Min. Mater. Proc. Inst. Jpn. 127, 132–138.
Murdoch, L.C., Hisz, D.B., Ebenhack, J.F., Fowler, D.E., Tiedeman, C.R., Germanovich, L.N., 2009. Analysis of hydromechanical well tests in fractured sedimentary rock at the NAWC Site, New Jersey. In: Proceedings of the 43rd US Rock Mechanics Symposium and 4th U.S.-Canada Rock Mechanics Symposium, ARMA 09-201. American Rock Mechanics Association, Asheville.
Nguyen, T.S., Guglielmi, Y., Graupner, B., Rutqvist, J., 2019. Mathematical modelling of fault reactivation induced by water injection. Minerals 9, 282. https://doi.org/10.3390/min9050282.
Niunoya, S., Matsui, H., 2007. The results of the investigation on rock mechanics in HDB-3–8 boreholes and study about the rock mechanical model around the Horonobe URL construction area. In: JAEA-Research 2006-086, Japan Atomic Energy Egency, Tokai-mura, Japan.
Nuclear Waste Management Program, 2011. nSIGHTS Version 2.41a User Manual. ERMS# 555653. Sandia National Laboratories, Carlsbad, New Mexico.
Pan, J.-B., Lee, C.-C., Lee, C.-H., Yeh, H.-F., Lin, H.-I., 2010. Application of fracture network model with crack permeability tensor on flow and transport in fractured rock. Eng. Geol. 116, 166–177.
Rinaldi, A.P., Rutqvist, J., 2019. Joint opening or hydroshearing? Analyzing a fracture zone stimulation at Fenton Hill. Geothermics 77, 83–98.
Rutqvist, J., 2015. Fractured rock stress-permeability relationships from in situ data and effects of temperature and chemical-mechanical couplings. Geofluids 15, 48–66.
Rutqvist, J., 2020. Thermal management associated with geologic disposal of large spent nuclear fuel canisters in tunnels with thermally engineered backfill. Tunn. Undergr. Space Technol. 102, 103454.
Rutqvist, J., Stephansson, O., 1996. A cyclic hydraulic jacking test to determine the in situ stress normal to a fracture. Int. J. Rock Mech. Min. Sci. Geomech. Abstr. 43, 695–711.
Rutqvist, J., Stephansson, O., 2003. The role of hydromechanical coupling in fractured rock engineering. Hydrogeol. J. 11, 7–40.
Rutqvist, J., Noorishad, J., Tsang, C.-F., Stephansson, O., 1998. Determination of fracture storativity in hard rocks using high-pressure injection testing. Water Resour. Res. 34, 2551–2560.
Rutqvist, J., Rinaldi, A.P., Cappa, F., Moridis, G.J., 2015. Modeling of fault activation and seismicity by injection directly into a fault zone associated with hydraulic fracturing of shale-gas reservoirs. J. Pet. Sci. Eng. 127, 377–386.
Sanada, H., Nakamura, T., Sugita, Y., 2010. In situ stress measurements in siliceous mudstones at Horonobe underground research laboratory, Japan. In: Proceedings of the ASME 13th International Conference on Environmental Remediation and Radioactive Waste Management. American Society of Mechanical Engineers, New York, pp. 31–39.
Sanada, H., Nakamura, T., Sugita, Y., 2012. Mine-by experiment in a deep shaft in Neogene sedimentary rocks at Horonobe, Japan. Int. J. Rock Mech. Min. Sci. 56, 127–135.
Schweisinger, T., Murdoch, L., Huey Jr., C., 2007. Removable borehole extensometers for measuring axial displacements during well tests. Geotech. Test. J. 30, 202–211.
Schweisinger, T., Svenson, E.J., Murdoch, L.C., 2009. Introduction to hydromechanical well tests in fractured rock aquifers. Ground Water 47, 69–79.
Schweisinger, T., Svenson, E.J., Murdoch, L.C., 2011. Hydromechanical behavior during constant-rate pumping tests in fractured gneiss. Hydrogeol. J. 19, 963–980.
Shahbazi, A., Saeidi, A., Chesnaux, R., 2020. A review of existing methods used to evaluate the hydraulic conductivity of a fractured rock mass. Eng. Geol. 265, 105438.
Snow, D.T., 1968. Rock fracture spacings, openings, and porosities. J. Soil Mech. Found. Div. 94, 73–92.
Sun, Z., Wang, L., Zhou, J.-Q., Wang, C., 2020. A new method for determining the hydraulic aperture of rough rock fractures using the support vector regression. Eng. Geol. 271, 105618.
Svenson, E., Schweisinger, T., Murdoch, L.C., 2007. Analysis of the hydromechanical behavior of a flat-lying fracture during a slug test. J. Hydrol. 347, 35–47.
Svenson, E., Schweisinger, T., Murdoch, L.C., 2008. Field evaluation of the hydromechanical behavior of flat-lying fractures during slug tests. J. Hydrol. 359, 30–45.
Tezuka, K., Niitsuma, H., 2000. Stress estimated using microseismic clusters and its relationship to the fracture system of the Hijiori hot dry rock reservoir. Eng. Geol. 56, 47–62.
Urpi, L., Rinaldi, A.P., Rutqvist, J., Wiemer, S., 2019. Fault stability perturbation by thermal pressurization and stress transfer around a deep geological repository in a clay formation. J. Geophys. Res. Solid Earth 124, 8506–8518.
Vilarrasa, V., Carrera, J., Olivella, S., Rutqvist, J., Laloui, L., 2019. Induced seismicity in geologic carbon storage. Solid Earth 10, 871–892.
Yoshino, H., Kishi, A., Yokota, H., 2015. Long-term pore-pressure-monitoring using deep boreholes in the Horonobe Underground Research Project. In: JAEA-Data/Code 2015-014, Japan Atomic Energy Agency, Tokai-mura, Japan, https://doi.org/10.11484/jaea-data-code-2015-014.
Zakharova, N.V., Goldberg, D.S., 2014. In situ stress analysis in the northern Newark Basin: implications for induced seismicity from CO_2 injection. J. Geophys. Res. Solid Earth 119, 2362–2374.
Zhan, S.-S., Wang, T.-T., Huang, T.-H., 2016. Variations of hydraulic conductivity of fracture sets and fractured rock mass with test scale: Case study at Heshe well site in Central Taiwan. Eng. Geol. 206, 94–106.
Zheng, B., Qi, S., 2016. A new index to describe joint roughness coefficient (JRC) under cyclic shear. Eng. Geol. 212, 72–85.